hostile environments as found near millisecond pulsars[29], it could well be that planet formation is now occurring in the stationary circumbinary disk of the evolved system HD44179.

There is direct evidence for the presence of magnesium-rich crystalline silicates in the proto-solar nebula, because crystalline enstatite (a magnesium-rich pyroxene) has been found in interplanetary dust particles[30]. It may very well be that these grains were produced in the outflows of evolved red giants and supergiants. However, so far no strong evidence for the presence of crystalline silicates in the ISM has been found. This implies that crystalline silicates may not be produced sufficiently abundant to be detected in the ISM, where they are mixed with other dust components. Alternatively, the crystalline grains may be destroyed in the ISM. The relatively high abundance of crystalline silicates observed in some proto-planetary disks[7] suggests that crystallization may also occur during the star formation and planet formation process. □

Received 3 November; accepted 14 December 1997.

1. Cohen, M. *et al.* The peculiar object HD44179 ("The Red Rectangle"). *Astrophys. J.* **196,** 179–189 (1975).
2. van Winckel, H., Waelkens, C. & Waters, L. B. F. M. The extremely iron-deficient "post-AGB" stars are binaries. *Astron. Astrophys.* **293,** L25–L28 (1995).
3. Roddier, F., Roddier, C., Graves, J. E. & Northcott, M. J. Adaptive optics imaging of proto-planetary nebulae: Frosty Leo and the Red Rectangle. *Astrophys. J.* **443,** 249–260 (1995).
4. Osterbart, R., Langer, N. & Weigelt, G. High resolution imaging of the bipolar nebula Red Rectangle. Evidence for unstable mass transfer in a close binary system. *Astron. Astrophys.* **325,** 609–612 (1997).
5. Bregman, J. D., Rank, D., Temi, P., Hudgins, D. & Kay, L. 3.3 and 11.3 micron images of HD44179—evidence for an optically thick polycyclic aromatic hydrocarbon disk. *Astrophys. J.* **411,** 794–796 (1993).
6. Sloan, G. C., Grasdalen, G. L. & Levan, P. D. Spatially resolved spectra of the unidentified infrared features around HD44179 (the Red Rectangle). *Astrophys. J.* **409,** 412–416 (1993).
7. Waelkens, C. *et al.* SWS observations of young main sequence stars with dusty circumstellar disks. *Astron. Astrophys.* **315,** L245–L248 (1996).
8. Russel, R. W., Soifer, B. T. & Willner, S. P. The infrared spectra of CRL618 and HD44179 (CRL915). *Astrophys. J.* **220,** 568–572 (1978).
9. Leger, A. & Puget, J. L. Identification of the 'undentified' IR emission features of interstellar dust? *Astron. Astrophys.* **137,** L5–L8 (1984).
10. Waelkens, C., van Winckel, H., Waters, L. B. F. M. & Bakker, E. J. Variability and nature of the Red Rectangle nebula. *Astron. Astrophys.* **314,** L17–L20 (1996).
11. Bond, H. E. Chemical compositions of post-AGB stars. in *Evolution of Stars: the Photospheric Abundance Connection* (eds Michaud, G. & Tutukov, A. V.) 341–349 (IAU Symp. 145, Kluwer, Dordrecht, 1991).
12. van Winckel, H., Mathis, J. & Welkens, C. Evidence from zinc abundances for dust fractionation in chemically peculiar stars. *Nature* **356,** 500–501 (1992).
13. Artymowitz, P. & Lubow, S. H. Mass flow through gaps in circumbinary disks. *Astrophys. J.* **467,** L77–L80 (1996).
14. De Graauw, Th. *et al.* Observing with the ISO Short-Wavelength Spectrometer. *Astron. Astrophys.* **315,** L49–L54 (1996).
15. Kessler, M. F. *et al.* The Infrared Space Observatory (ISO) mission. *Astron. Astrophys.* **315,** L27–L31 (1996).
16. Beintema, D. A. *et al.* The rich spectrum of circumstellar PAHs. *Astron. Astrophys.* **315,** L369–L372 (1996).
17. Waters, L. B. F. M. *et al.* Mineralogy of oxygen-rich dust shells. *Astron. Astrophys.* **315,** L361–L364 (1996).
18. Koike, C., Shibai, H. & Tuchiyama, A. Extinction of olivine and pyroxene in the mid- and far-infrared. *Mon. Not. R. Astron. Soc.* **264,** 654–658 (1993).
19. Jäger, C., Mutschke, H., Begemann, B., Dorschner, J. & Henning, Th. Steps toward interstellar silicate mineralogy. 1: Laboratory results of a silicate glass of mean cosmic composition. *Astron. Astrophys.* **292,** 635–641 (1994).
20. Omont, A. *et al.* Observations of 40–70 micron bands of ice in IRAS09371 + 1212 and other stars. *Astrophys. J.* **355,** L27–L30 (1990).
21. van der Veen, W. E. C. J., Waters, L. B. F. M., Trams, N. R. & Matthews, H. E. A study of dust shells around high latitude supergiants. *Astron. Astrophys.* **285,** 551–564 (1994).
22. Jura, M., Turner, J. & Balm, S. P. Big grains in the Red Rectangle? *Astrophys. J.* **474,** 741–748 (1997).
23. Reese, M. D. & Sitko, M. L. Ultraviolet and visible spectropolarimetry of the Red Rectangle and HD44179. *Astrophys. J.* **467,** L105–L108 (1996).
24. Willems, F. J. & de Jong, T. Carbon stars with oxygen-rich dust shells: Evidence for the onset of the carbon star phase. *Astrophys. J.* **309,** L39–L42 (1986).
25. Morris, M. Mechanisms for mass loss from cool stars. *Publ. Astron. Soc. Pacif.* **99,** 1115–1122 (1987).
26. Lopez, B., Tessier, E., Cruzalebes, P., Lefevre, J. & Le Bertre, T. Dust envelope modelling of the Red Rectangle nebula. *Astron. Astrophys.* **322,** 868–877 (1997).
27. Jura, M., Balm, S. P. & Kahane, C. A long-lived disk around the Red Rectangle? *Astrophys. J.* **453,** 721–726 (1995).
28. Mannings, V., Koerner, D. W. & Sargent, A. I. A rotating disk of gas and dust around a young counterpart to β Pictoris. *Nature* **388,** 555–557 (1997).
29. Wolszczan, A. & Frail, D. A. A planetary system around the millisecond pulsar PSR1257 + 12. *Nature* **355,** 145–147 (1992).
30. Bradley, J. P., Brownlee, D. E. & Veblen, D. R. Pyroxene whiskers and platelets in interplanetary dust: evidence of vapour phase growth. *Nature* **301,** 473–477 (1983).

Acknowledgements. We thank H. Dorschner for providing the laboratory spectrum of olivine. L.B.F.M.W., A.dK. and J.B. acknowledge financial support from an NWO 'Pionier' grant. F.J.M. acknowledges support from an NWO project grant. C.W. acknowledges financial support from the Belgian Federal Services for Scientific, Technological and Cultural Affairs, and from the Onderzoeksfonds K.U. Leuven. H.V.W. acknowledges financial support from the Fund for Scientific Research of Flanders. We thank A. Boogert for discussions on the CO_2 bands in the Red Rectangle.

Correspondence and requests for materials to L.B.F.M.W. (e-mail: rensw@astro.uva.nl).

Dephasing in electron interference by a 'which-path' detector

E. Buks, R. Schuster, M. Heiblum, D. Mahalu & V. Umansky

Braun Center for Submicron Research, Department of Condensed Matter Physics, Weizmann Institute of Science, Rehovot 76100, Israel

Wave–particle duality, as manifest in the two-slit experiment, provides perhaps the most vivid illustration of Bohr's complementarity principle: wave-like behaviour (interference) occurs only when the different possible paths a particle can take are indistinguishable, even in principle[1]. The introduction of a which-path (*welcher Weg*) detector for determining the actual path taken by the particle inevitably involved coupling the particle to a measuring environment, which in turn results in dephasing (suppression of interference). In other words, simultaneous observations of wave and particle behaviour is prohibited. Such a manifestation of the complementarity principle was demonstrated recently using a pair of correlated photons, with measurement of one photon being used to determine the path taken by the other and so prevent single-photon interference[2]. Here we report the dephasing effects of a which-path detector on electrons traversing a double-path interferometer. We find that by varying the sensitivity of the detector we can affect the visibility of the oscillatory interference signal, thereby verifying the complementarity principle for fermions.

Mesoscopic systems[3] can be used to study the interplay between interference and dephasing of electrons[4]. Nano-scale fabrication and low-temperature measuring techniques, which minimize unintentional dephasing, enable the observation of variety of coherent effects of electrons such as an induced Aharonov–Bohm phase, weak localization, resonant tunnelling and conductance quantization[3]. A controllable dephasing via a which-path detector, on the other hand, has not been previously demonstrated in such systems.

In our experiment we used a double-path electronic interferometer[5], fabricated within the plane of a high-mobility two-dimensional electron gas. The two paths are defined by two slits electrons can pass through, with one slit in the form of a coherent quantum dot (QD)[5,6]. The QD is a trap that captures electrons for a relatively long time, like a resonant delay line, thus allowing the electrons to be detected more easily. Near the QD, but electrically separated from it, a quantum point contact (QPC) is fabricated, serving as a which-path detector. The QPC is a short conducting segment with width comparable to the electron wavelength, allowing only a small number of modes to pass. It is expected that an electron passing the QD-slit will interact with the nearby QPC-detector (both systems are thus 'entangled'[7]) and modify the conductance of the QPC[8]. This detection process leads to dephasing, that is, to a suppression of the double-path Aharanov–Bohm interference.

The two-path interferometer (Fig. 1) consists of emitter E and collector C constrictions; each constriction is made by a single-mode QPC, and there is a base region B between them. The grounded base contacts (with voltage $V_B = 0$) serve as draining reservoirs for back-scattered electrons, ensuring that only two forward-propagating paths reach the collector. The emitter is separated from the collector by a barrier with two slits; one of those slits is a QD. As the collector signal is small, we incorporated additional reflecting barriers (the white gates in Fig. 1a) to direct the emitted electrons into the two slits and subsequently to reflect them towards the collector. All measurements were done at an electrons demonstration of the AB effect:

temperature $\Theta \approx 80\,\text{mK}$ and an a.c. emitter excitation voltage $V_E = 10\,\mu\text{V}$. Under these conditions both coherence length (due to unintentional dephasing) and mean free path for elastic scattering of the electrons exceed the entire size of the interferometer.

The collector current is related to the transmission probability from emitter to collector, T_{EC}, via the multiprobe conductance formula[9], $I_C = (2e^2/h)T_{EC}V_E$. As stressed above, the dominant contribution to T_{EC} comes from the two direct paths, those going from E to C through the two slits (depicted by the two dotted lines in Fig. 1a; longer paths, resulting from multiple reflections from walls, are much less probable. A phase difference between the two direct paths, $\Delta\alpha = 2\pi\Phi/\Phi_0$, is induced via the Aharonov–Bohm effect (for a review see ref. 10). Here Φ is the magnetic flux threaded through the area, A, enclosed by these two paths and $\Phi_0 = h/e$ is the flux quantum. Consequently, the collector current oscillates as a function of magnetic field B with a period $\Delta B = \Phi_0/A = 2.6\,\text{mT}$, corresponding to a phase difference between the two paths equal to 2π, as seen in Fig. 2a.

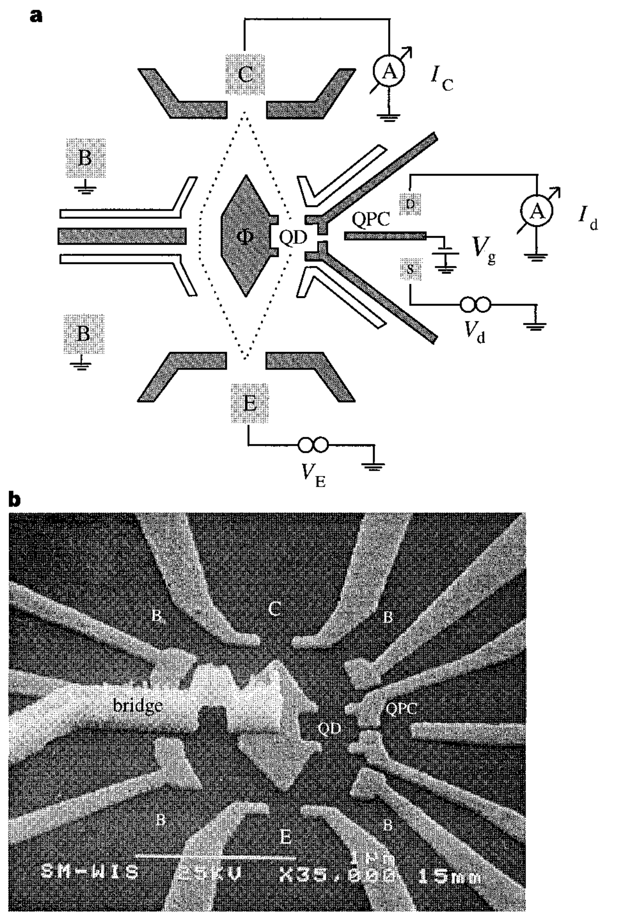

Figure 1 The which-path device. **a**, Schematic description of the top electrodes and contacts of the interferometer and the detector. The interferometer is composed of three different regions, emitter E, collector C, and base B. The right slit is in a form of a quantum dot, QD (with area $0.4 \times 0.4\,\mu\text{m}^2$) with a quantum point contact, QPC, on its right side serving as a which-path detector. The excitation voltage V_E is applied between emitter and base. **b**, Top-view scanning electron micrograph of the device. Scale bar, $1\,\mu\text{m}$. The GaAs-AlGaAs heterostructure supports a high-mobility two-dimensional electron gas (2DEG) (with density $n_s = 3.0 \times 10^{11}\,\text{cm}^{-2}$ and low-temperature mobility $\mu = 2.8 \times 10^6\,\text{cm}^2\,\text{V}^{-1}\,\text{s}^{-1}$) formed 60 nm beneath the surface. Potential barriers and narrow openings in the plane of the 2DEG are induced by negatively biased miniature metal gates deposited on the surface of the heterostructure, thus depleting the electrons underneath the gates. A special lithographic technique, involving a metallic air bridge, is used to contact the central gate that depletes the area between the two slits (this serves also as plunger gate of the QD).

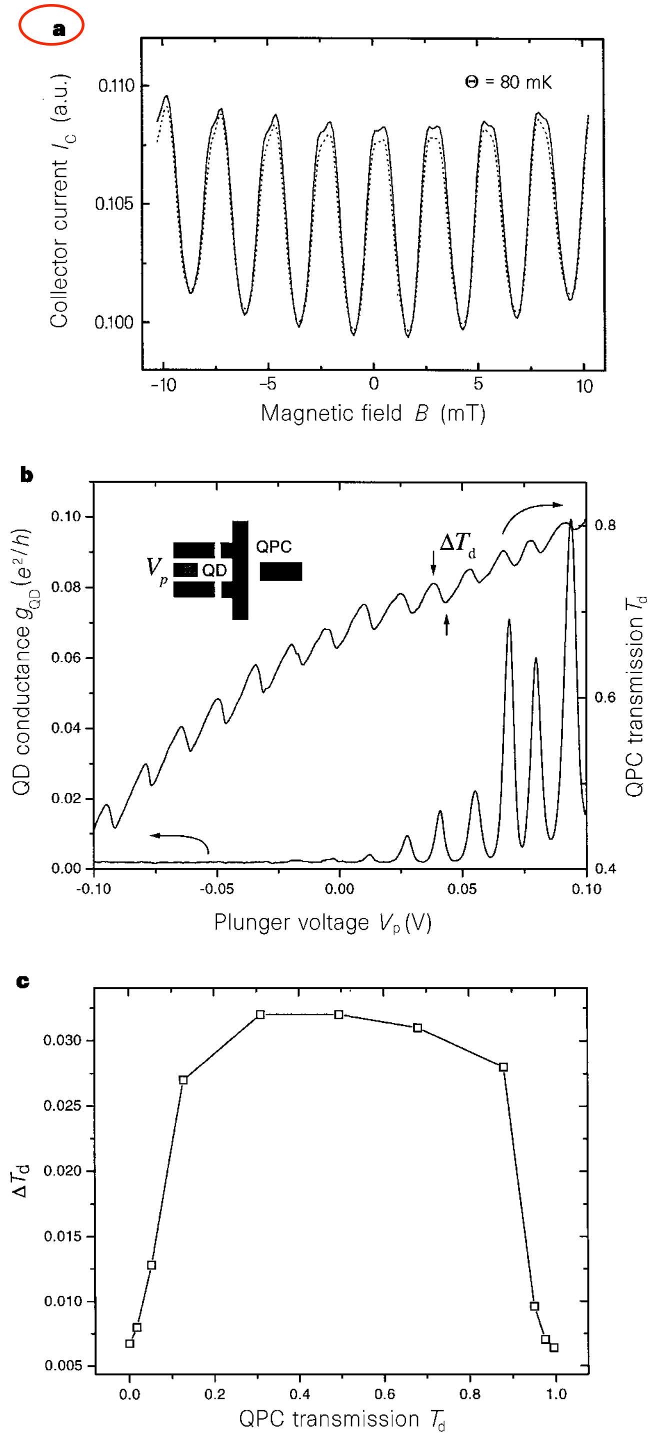

Figure 2 Conduction characteristics of the which-path device. **a**, Aharonov–Bohm oscillations of the collector current I_C with a period $\Delta B = \Phi_0/A = 2.6\,\text{mT}$. The solid line is measured with QPC drain source voltage $V_d = 0$ (which-path detector turned off), while the dotted line, with a reduced visibility, is measured with $V_d = 100\,\mu\text{eV}$. (a.u., arbituary units.) **b**, The conductance of the QD, g_{QD}, and the transmission of the QPC nearby, T_d, as a function of the plunger gate voltage, V_p. The inset shows schematically the coupled structures. **c**, The induced average change in the transmission probability of the QPC detector, ΔT_d, due to adding an electron to the QD as a function of T_d. ΔT_d is calculated by averaging over several coulomb-blockage peaks. The reduced value of ΔT_d near $T_d = 0$ and $T_d = 1$ is a consequence of approaching the conductance plateaus.

The suppression of Ahoronov–Bohm oscillations due to the which-path detector depends on the effect an electron dwelling in the QD has on the detector. We study the QD–QPC interaction by means of a calibration device (seen in Fig. 2b inset), fabricated on the same wafer, containing a QD and a QPC similar to these in the which-path interferometer. The QD is tuned to the coulomb blockade regime, having therefore well separated energy levels, by adjusting the resistance of each of its two QPCs to be greater than $h/2e^2$. Each peak in the conductance of the QD, scanned by the plunger gate voltage V_p (see Fig. 2b), is associated with adding a single electron in the QD. Owing to the proximity between the QD and QPC, the transmission probability of the QPC-detector T_d, and thus its conductance $g_d = (2e^2/h)T_d$, are affected by the potential of the QD[8]. As the plunger gate voltage is being scanned between two adjacent conductance peaks, with fixed charge in the QD, the potential of the QD changes smoothly. However, when a conductance peak is being scanned, with an electron being added to the QD, a faster and opposite change in the potential of the QD takes place, on the scale of the peak width. Consequently, the potential of the QPC, and therefore T_d, are expected to show a saw-tooth-like oscillations (with amplitude ΔT_d), as indeed observed in the experimental results in Fig. 2b (see also ref. 8).

We now consider the expected quantitative dephasing induced by the WP detector. This has been treated recently by Aleiner *et al.*[11], Levinson[12], Gurvitz[13], and Imry[14]. Following ref. 4, we write the entangled wavefunction of the whole system (interferometer + detector) as:

$$|\psi\rangle = |\phi_l\rangle_e \otimes |\chi_l\rangle_d + e^{i\Delta\alpha}|\phi_r\rangle_e \otimes |\chi_r\rangle_d \qquad (1)$$

where $|\phi_l\rangle_e$ ($|\phi_r\rangle_e$) is the electronic partial wave in the left (right) path, and $|\chi_l\rangle_d$ ($|\chi_r\rangle_d$) represents the state of the detector coupled to the left (right) partial electronic wave. The probability to find the electron at the collector is found by summing over all possible states of the detector (as the collector is sensitive only to the electron position, regardless the state of the detector), $T_{EC} = \Sigma_i |\langle\psi|\mathbf{r}_C\rangle_e \otimes |\chi_i\rangle_d|^2$ where $|\mathbf{r}_C\rangle_e$ represents the state of an electron at the collector. Assuming $|\chi_l\rangle_d$ and $|\chi_r\rangle_d$ are normalized one finds:

$$T_{EC} = |_e\langle\phi_l|\mathbf{r}_C\rangle_e|^2 + |_e\langle\phi_r|\mathbf{r}_C\rangle_e|^2 + 2\mathrm{Re}[e^{i\Delta\alpha}\, {}_e\langle\phi_l|\mathbf{r}_C\rangle_e \cdot {}_e\langle\mathbf{r}_C|\phi_r\rangle_e \cdot {}_d\langle\chi_r|\chi_l\rangle_d] \qquad (2)$$

(where Re denotes real part) with the visibility of the interference pattern,defined as the peak-to-valley value normalized by the average value, being proportional to:

$$\nu_d = |_d\langle\chi_r|\chi_l\rangle_d| \qquad (3)$$

Here ν_d represents which-path information that can be obtained from the detector[15], namely, the smaller ν_d is, the stronger is the dephasing and the weaker is the visibility. In the extreme case, when the detector determines unambiguously where the electron is, both detector states $|\chi_l\rangle_d$ and $|\chi_r\rangle_d$ are orthogonal and the Ahoronov–Bohm interference vanishes.

How certain is our which-path detection? An electron entering the QD-slit changes the transmission probability of the QPC-detector by ΔT_d. The rate at which particles probe the detector at zero temperature is $2eV_d/h$, where V_d is the voltage across the detector. Thus, the number of particles probing the detector during the dwell time of the electron in the QD, $\tau_d = h/2\pi\Gamma$ (Γ is the elastic width of the resonant state), is $N = \tau_d 2eV_d/h = (1/\pi)eV_d/\Gamma$. Now, we let N_t be the number of transmitted particles out of the total N particles probing the detector. This is a binomial random variable (leading to 'shot noise' in the current), having an expectation value $\langle N_t\rangle = NT_d$ and a standard deviation $\sigma(N_t) = \sqrt{NT_d(1-T_d)}$ (refs 16, 17). To determine the certitude of the detection and thus the extent of dephasing, ΔT_d has to be compared with the resultant uncertainty in T_d, given by $\sigma(T_d) = \sqrt{T_d(1-T_d)/N}$. For a noisy detector, $\sigma(T_d) \gg \Delta T_d$: the detector does not provide which-path information and one expects distinct interference, namely $\nu_d \approx 1$. Whereas for a quiet detector, $\sigma(T_d) \ll \Delta T_d$: one can determine, even if 'in principle', the path the electron takes, and consequently, the interference pattern is expected to diminish.

A direct evaluation of the overlap ν_d in equation (3), for a symmetric barrier in the QPC detector[11], leads to $\nu_d = 1 - (1/8)[\Delta T_d/\sigma(T_d)]^2$ at zero temperature, namely:

$$\nu_d = 1 - \frac{1}{\pi}\frac{eV_d}{\Gamma}\frac{(\Delta T_d)^2}{8T_d(1-T_d)} \qquad (4)$$

We measured the visibility of the Ahoronov–Bohm oscillations when the QD-slit is tuned to a conduction peak (using the central

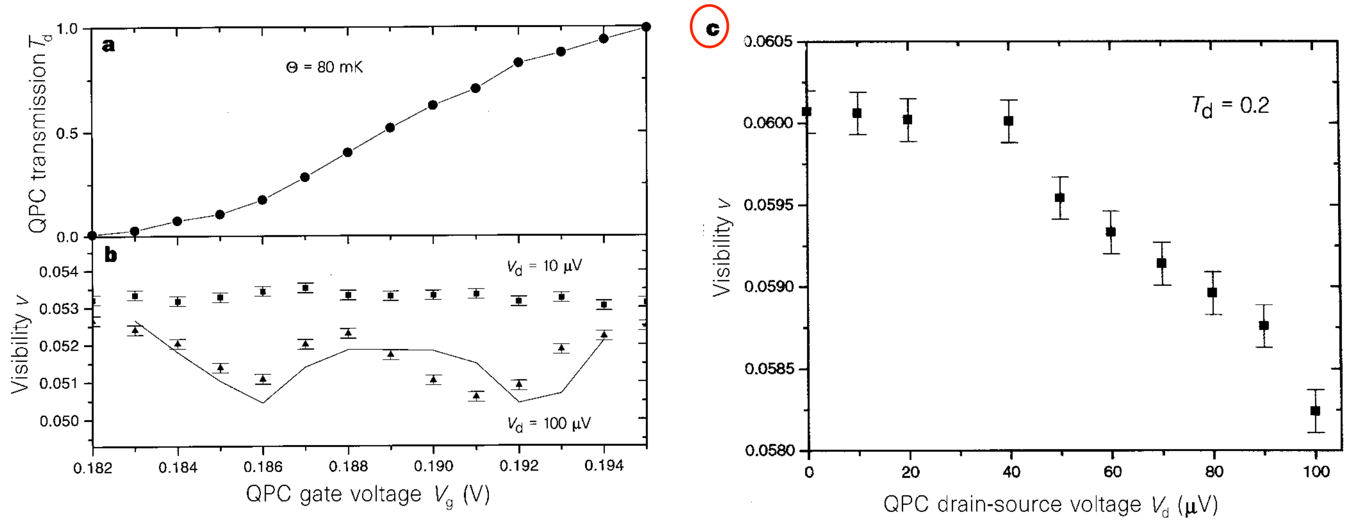

Figure 3 Measurements of visibility. **a**, The transmission probability of the QPC detector, T_d, as a function of the voltage applied to the right gate of the QPC-detector, V_g. **b**, The visibility (ν) of the Ahoronov–Bohm (AB) oscillations as a function of V_g for two values of drain source voltage, V_d. The peak-to-valley value of the AB oscillations is obtained using the following procedure. First, the non-oscillatory component of the trace I_C versus B is subtracted using a least-mean-squared fit to a polynomial of degree 2. Second, numerical integration of the remaining oscillatory component squared leads to the peak-to-valley value. Last, the visibility is found by dividing by the average value of I_C. Error bars indicate the fluctuations in visibility due to fluctuations of device's properties (instrumental noise is negligibly small). **c**, The visibility of the AB conductance oscillations as a function of V_d for a fixed $T_d = 0.2$. The behaviour is linear for $eV_d > k_B\Theta$ with saturation for low V_d.

metal island as a plunger gate), and the QPC-detector conducting current with transmission $0 \leqslant T_d \leqslant 1$. Figure 3a shows the transmission probability of the QPC detector, T_d, and Fig. 3b shows the visibility for two values of V_d, both as a function of V_g (see Fig. 1a). For $V_d = 100\,\mu V$ the observed visibility peaks when ΔT_d of the QPC-detector is small near conductance plateaus, and also near $T_d = 0.5$, with the quantum shot noise in the QPC-detector at maximum. In these regimes the which-path detector provides least-certain information about the location of the electron and therefore dephasing is small. These features disappear when V_d is reduced to $10\,\mu V$. This observation confirms that the behaviour of the visibility found for $V_d = 100\,\mu V$ is indeed due to dephasing, and is not related to undesirable electrostatic effect of V_g on the QD.

To compare our experimental results for the case $V_d = 100\,\mu V$ with theory, we use the zero-temperature value of ν_d in equation (4) (valid because $eV_d \gg k_B\Theta \approx 7\,\mu eV$ (E.B., unpublished results). We use the measured ΔT_d in the calibration device (see Fig. 2c) and a value $\Gamma = 0.5\,\mu eV$ (corresponding to $\tau_d \approx 1.3$ ns) as a fitting parameter. The calculated visibility, drawn as a solid line in Fig. 3b, shows reasonable agreement with experiment, both qualitatively and quantitatively. The dependence of the visibility on drain source voltage V_d (measured in a different working regime from that shown in Fig. 3b) is given in Fig. 3c. For $eV_d \gg k_B\Theta$, the visibility drops linearly as the probing rate of the QPC-detector by the electrons increases, as expected from equation (4). The deviation from the linear dependence near $V_d = 0$ can be accounted for by the fact that $eV_d \approx k_B\Theta$ (E.B., unpublished results).

Apart from demonstrating the principle of complementarity, we believe that similar experimental set-ups, but with higher detector sensitivity, may be used to study other fundamental problems in quantum mechanics. For example, looking at the current of the which-path detector in the time domain may shed light on the old and controversial issue of wavefunction collapse. Moreover, increasing the mutual coupling between detector and interferometer might open a way to fabrication of an electronic quantum bit, with possible applications in quantum computing. □

Received 17 September; accepted 16 December 1997.

1. Bohr, N. in *Albert Einstein: Philosopher—Scientist* (ed. Schilpp, P. A.) 200–241 (Library of Living Philosophers, Evanston, 1949).
2. Zou, X. Y., Wang, L. J. & Mandel, L. Induced coherence and indistinguishability in optical interference. *Phys. Rev. Lett.* **67,** 318–321 (1991).
3. Imry, Y. *Introduction to Mesoscopic Physics* (Oxford Univ. Press, 1997).
4. Stern, A., Aharonov, Y. & Imry, Y. Phase uncertainty and loss of interference: a general picture. *Phys. Rev. A* **41,** 3436–3448 (1990).
5. Schuster, R. *et al.* Phase measurement in a quantum dot via a double-slit interference experiment. *Nature* **385,** 417–420 (1997).
6. Van Houten, H., Beenakker, C. W. J. & Staring, A. A. W. in *Single Charge Tunneling—Coulomb Blockade Phenomena in Nanostructures* (eds Grabert, H. & Devoret, M. H.) Ch. 5 (Plenum, New York, 1992).
7. Gurvitz, S. A. Interaction free measurement in mesoscopic systems and the reduction postulate. Preprint available at http://xxx.lanl.gov/abs/quant-ph/9607029.
8. Field, M. *et al.* Measurements of Coulomb blockade with a noninvasive voltage probe. *Phys. Rev. Lett.* **70,** 1311–1314 (1993).
9. Buttiker, M. Four terminal phase coherent conductance. *Phys. Rev. Lett.* **57,** 1761–1764 (1986).
10. Aronov, A. G. & Sharvin, Yu. V. Magnetic flux effects in disordered conductors. *Rev. Mod. Phys.* **59,** 755–779 (1987).
11. Aleiner, I. L., Wingreen, N. S. & Meir, Y. Dephasing and the orthogonality catastrophe in tunneling through a quantum dot: the "which path?" interferometer. *Phys. Rev. Lett.* **79,** 3740–3743 (1997).
12. Levinson, Y. Dephasing in a quantum dot due to coupling with a quantum point contact. *Europhys. Lett.* **39,** 299–304 (1997).
13. Gurvitz, S. A. Measurements with a noninvasive detector and dephasing mechanism. *Phys. Rev. B* **56,** 15215–15223 (1997).
14. Imry, Y. in *Proc. 1997 Nobel Symp. on Modern Studies of Basic Quantum Concepts and Phenomena* (in the press).
15. Eglert, B. G. Fringe visibility and which-way information: an inequality. *Phys. Rev. Lett.* **77,** 2154–2157 (1996).
16. Khlus, V. A. Current and voltage fluctuations in microjunctions between normal metals and superconductors. *JETP* **66,** 1243–1249 (1987).
17. Lesovik, G. B. Excess quantum noise in 2D ballistic point contacts. *JETP Lett.* **49,** 592–594 (1989).

Acknowledgements. We thank S. Gurvitz for presenting to us ref. 7, which initiated the present work. We also thank I. Imry, Y. Levinson, Y. Meir, A. Stern and N. Wingreen for discussions. This work was supported in part by a MINERVA grant and a MINERVA fellowship for one of us (R.S.).

Correspondence and requests for materials should be addressed to M.H. (e-mail address: heiblum@wis.weizmann.ac.il).

Two-dimensional ferroelectric films

A. V. Bune*†, V. M. Fridkin*†, Stephen Ducharme*, L. M. Blinov†, S. P. Palto†, A. V. Sorokin†, S. G. Yudin† & A. Zlatkin†

* *Department of Physics and Astronomy and the Center for Materials Research and Analysis, University of Nebraska, Lincoln, Nebraska 68588-0111, USA*
† *Institute of Crystallography of the Russian Academy of Sciences, 117 333 Moscow, Russia*

Ultrathin crystalline films offer the possibility of exploring phase transitions in the crossover region between two and three dimensions. Second-order ferromagnetic phase transitions have been observed in monolayer magnetic films[1,2], where surface anisotropy energy stabilizes the two-dimensional ferromagnetic state at finite temperature[3]. Similarly, a number of magnetic materials have magnetic surface layers that show a second-order ferromagnetic–paramagnetic phase transition with an increased Curie temperature[4]. Ferroelectricity is in many ways analogous to ferromagnetism, and bulk-like ferroelectricity and finite-size modifications of it have been seen in nanocrystals as small as 250 Å in diameter[5], in perovskite films 100 Å thick[6] and in crystalline ferroelectric polymers as thin as 25 Å (refs 7–10). But these results can be interpreted as bulk ferroelectricity suppressed by surface depolarization energies, and imply that the bulk transition has a minimum critical size[11–13]. Here we report measurements of the ferroelectric transition in crystalline films of a random copolymer of vinylidene fluoride and trifluoroethylene just 10 Å (two monolayers) thick. We see a first-order ferroelectric phase transition with a transition temperature nearly equal to the bulk value, even in these almost two-dimensional films. In addition, we see a second first-order transition at a lower temperature, which seems to be associated with the surface layers only. The near-absence of finite-size effects on the bulk transition implies that these films must be considered as two-dimensional ferroelectrics.

Ferroelectric polymers have been studied in great detail for nearly 30 years and are in wide use in a variety of piezoelectric devices[14,15]. One of the most interesting systems is the random copolymer of vinylidene fluoride with trifluoroethylene, P(VDF-TrFE) (ref. 16), consisting of $-((-CF_2-CH_2)_x-(-CF_2-CHF-)_{1-x})_n-$ chains with a regular intra-chain period of 2.6 Å, controlled by the C–C bonds between fluorine pairs, as shown in Fig. 1a. In the ferroelectric phase, the all-*trans* chains are arranged in parallel rows in a quasi-hexagonal close packing with orthorhombic *mm*2 structure[17]. P(VDF-TrFE 70:30) has a first-order ferroelectric–paraelectric phase transition (connected with the conversion of all-*trans* chains to mixtures of *trans* and *gauche* bonds with little or no net dipole moment[16]) with Curie temperature $T_c \approx 100\,°C$ (the Curie temperature increases with the proportion of the VDF component), thermal hysteresis of $\Delta T_c \approx 20\,°C$, and a spontaneous polarization $P_s \approx 0.1\,C\,m^{-2}$ at room temperature[16]. Thin films have usually been formed by solvent spinning and are polymorphous, containing amorphous material and incompletely orientated crystallites. Finite-size effects were evident from an increase in the coercive field in films as thin as 600 Å (ref. 18).

The first crystalline Langmuir–Blodgett-deposited polymer films, of P(VDF-TrFE 70:30), achieved a great improvement in quality[7,8,10]. They have excellent crystalline order and show the first-order ferroelectric–paraelectric transition at $T_c \approx 80\,°C$ on cooling. These ferroelectric polymer films, 30 monolayers (ML) thick (~150 Å), also showed double hysteresis and the critical point[19], and a new conductance switching controlled by the polarization state[8]. Finite-size effects have been demonstrated in these films; the